Measurement 184 (2021) 109910

Contents lists available at ScienceDirect

Measurement

journal homepage: www.elsevier.com/locate/measurement

Fractal dimension for bending–torsion fatigue fracture characterisation

Wojciech Macek [a,*], Ricardo Branco [b], Mateusz Korpyś [c], Tadeusz Łagoda [d]

[a] Gdańsk University of Technology, Faculty of Mechanical Engineering and Ship Technology, 11/12 Gabriela Narutowicza, Gdańsk 80-233, Poland
[b] University of Coimbra, CEMMPRE, Department of Mechanical Engineering, Rua Luís Reis Santos, Coimbra 3030-788, Portugal
[c] Polish Academy of Sciences, Institute of Chemical Engineering, Bałtycka 5, Gliwice 44-100, Poland
[d] Opole University of Technology, Faculty of Mechanical Engineering, 5 Mikolajczyka Street, Opole 45-271, Poland

ARTICLE INFO

Keywords:
Fractography
Fractal dimension
Bending with torsion
Steel
Aluminium alloy

ABSTRACT

Fracture surfaces after biaxial fatigue tests were compared using fractal dimension for three types of metallic materials in smooth and notched specimens made of S355J2 and 10HNAP steels and 2017-T4 aluminium alloy, considering both proportional and nonproportional cyclic loading. High-resolution optical 3D measurement studies were performed on the entire fracture surface. A direct correlation between fractal dimension and fatigue loading was established. This systematic relationship can serve as a basis for obtaining information about fatigue loading from the fracture surfaces of failed materials and structures. Moreover, measurements of the fracture surface with an optical profilometer, quantitative analysis, and fractography contribute to a better comprehension of the fatigue failure processes. Differences in individual zones of fatigue fractures were identified while demonstrating the correctness of the total fracture surface method.

1. Introduction

Fractographic investigation is one of the main engineering tools in the damage analysis of metal elements because it makes possible the correlation of fracture mechanisms and microscopic events with mechanical properties and material behaviour [1,2]. In the case of fatigue fracture, the relationship between failure mechanisms and service loadings is of great scientific interest [3–8]. However, most fractographic studies are limited to a visual description of fracture surfaces; therefore, this assessment is only established in a qualitative manner, even if observations are made at different length scales, which can vary from macro to nano scales.

Different observation methods can be used. The continuous improvement of methods and devices for measuring surface characteristics facilitates the increasingly accurate quantitative analysis of surface morphology [9–14]. Scanning electron microscopy (SEM) technique, which is one of the most popular techniques for the observation of material structures [15–19], can obtain resolutions higher than 1 nm. Another alternative technique for fractography analysis is plasma-focused ion beam scanning electron microscopy (PFIB-SEM). Fig. 1 presents, as an example, a micrograph of a 10HNAP specimen obtained by the first author using PFIB-SEM technique. It can be used to create cross sections of the surface [20–22] with large volumes while maintaining a high-resolution SEM image. Nevertheless, optical-based methods are the most popular approaches [14,23–25]. As reported by Townsend et al. [26], it provides a balance between the accuracy of the results, simplicity of operation, and processing time.

Fractographic techniques based on the total fracture area have been used in various scientific fields for quantitative failure analysis, for the characterisation of either ductile or brittle materials [27,2829,3031]. Quinn published a comprehensive guide focused on failure analysis of ceramics and glasses [31]. The book includes a multitude of practical examples and a detailed and extensive literature review. Very few studies on fractography analysis have been conducted on ductile materials subjected to bending–torsion loading [14,32–35]. Slámečka et al. [51] investigated the changes in profile roughness parameters for high-strength low-alloy steels and reported an important effect of torsion loading on surface topology. Later, the same authors [32] studied fish-eye crack formation using quantitative fractography analysis in nitrided high-strength steel. More recently, Macek et al. [28] addressed the effect of the normal stress to shear stress ratio on fracture surfaces in both conventional and additively manufactured high-strength steels. In both cases, fracture surface topography parameters and von Mises stress were successfully correlated via linear functions.

The fractal dimension is a powerful engineering tool that makes possible the correlation between geometrical irregularities and material properties. Since 1984, when Mandelbrot [36,37] introduced fractal

* Corresponding author.
E-mail address: wojciech.macek@yahoo.com (W. Macek).

https://doi.org/10.1016/j.measurement.2021.109910
Received 14 May 2021; Received in revised form 24 June 2021; Accepted 18 July 2021
Available online 30 July 2021

Nomenclature

A_{10} %	elongation
Df	fractal dimension
E GPa	Young's modulus
r	loading parameter
R	stress ratio
RA %	reduction of area
σ_a MPa	nominal normal stress amplitude
σ_{max} MPa	maximum normal stress
σ_u MPa	ultimate tensile strength
σ_y MPa	yield strength
τ_a MPa	nominal shear stress amplitude
τ_{max} MPa	maximum shear stress
ν	Poisson's ratio

analysis, much research has been conducted [32–36] on this subject. In particular, in the context of fracture, some studies focused on the relationship between microstructure features and fracture toughness or fracture energy. More recently, Hilders and Zambrano [43] identified a linear correlation between the impact toughness and the fractal dimensional increment for a super duplex stainless steel at room temperature. Tang and Wang [44] concluded that the roughness of the impact fracture surface can be addressed using a fractal approach. Venkatesh et al. [45] also found a linear relationship between the fractal dimension and fracture surface roughness. Fu et al. [46] applied the fractal dimension to study hydrogen embrittlement phenomena in transformation-induced plasticity steels and found linear correlations between the fractal parameters and hydrogen embrittlement susceptibility. With regard to monotonic properties, a direct relationship between the ultimate tensile strength and the fractal dimension of primary Mg_2Si particles in Al–Mg–Si matrix alloy composites was also reported by Akrami et al. [47].

With regard to fatigue fracture, little work has been done on the interconnection between fractal dimension and loading history [33,38–42,45]. To the best of the authors' knowledge, comparative studies on steel and aluminium alloys subjected to multiaxial loading are not available in literature. Therefore, this study aims to examine the correlation between the fractal dimension and fatigue loading for different steel and aluminium alloys. Notched and smooth samples with circular and rectangular cross sections were considered. Fatigue tests were conducted for proportional and nonproportional cyclic loading.

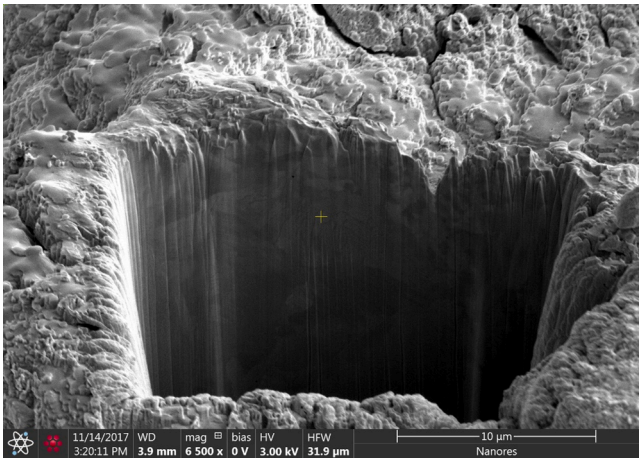

Fig. 1. Cross-sectional image taken by the first author using a microscope equipped with a dual-beam PFIB-SEM source for a 10HNAP specimen fracture with a magnification of 6500x.

From a broader perspective, considering all the trends of quantitative research, the availability of optical methods, and the variety of materials, shapes, and loads, an attempt was made to find a universal and simple method to identify the reasons for the destruction.

2. Materials and methods

2.1. Materials

The materials utilised in this study were 10HNAP and S355J2 steels and 2017-T4 aluminium alloy. Their chemical compositions and main mechanical properties can be seen in the paper by the authors [48]. The materials mentioned above were derived from different standards. Here, for the sake of simplicity, they are identified as 10HNAP, S355J2, and 2017-T4, respectively. The purpose of this combination of materials was to test the procedure for a wide variety of cases.

Regarding the microstructure features, optical micrographs taken with relatively high magnifications are exhibited in Fig. 2 for the three tested materials. The 10HNAP steel is a low-alloy structural steel consisting of a fine-grained ferritic-perlitic structure. The predominance of ferrite is visible by the white grains in the structure (see Fig. 2(a)) and the average grain diameter was equal to 22.5 µm. The microstrcture of the 2017-T4 aluminium alloy, as shown in Fig. 2(b), is composed by elongated grains of α solid solution of various sizes and widths up to about 40 µm. Between the elongated grains, there are clusters of very fine, equiaxed grains of the α phase in a band pattern. The S355J2 steel is a high-strength low-alloy steel formed by a ferrite-pearlite matrix with low pearlite content and had an average grain size of 15.9 µm (see Fig. 2 (c)). Average grain sizes were determined using the Jeffries method based on the ASTM E 112–12 standard.

2.2. Specimen geometries

Fig. 3 shows the specimen geometries, with dimensions in millimetres, tested in this research. The analysis included two notched geometries and one smooth geometry — more specifically, a V-notched round bar made of 10HNAP steel, as shown in Fig. 3(a), a smooth round bar made of S355J2 steel, as shown in Fig. 3(b), and a rectangular cross-section bar with a V-notch made of 2017-T4 aluminium alloy, as shown in Fig. 3(c). The notched angles were 60°. These geometries enable the methodology to be tested under different stress concentration conditions.

2.3. Fatigue tests

Fatigue tests were conducted in an MZGS-100 fatigue machine, as shown in Fig. 4, for three types of loading [49,50]: (1) pure bending, (2) combined torsion with bending, and (3) pure torsion. Both proportional loading and nonproportional loading were considered, as well as constant-amplitude and random loading histories. These loading scenarios were defined to test the procedure for different loading cases. To compare the different cases, the loading parameter, r, defined by the following equation, was introduced.

$$r = \frac{\tau_{max}}{\sigma_{max} + \tau_{max}} \tag{1}$$

where τ_{max} and σ_{max} are the maximum shear stress and maximum normal stress, respectively. From the analysis of Eq. (1), one can conclude that $r = 0$ is associated with pure bending, $r = 1$ is associated with to pure torsion, and $0 < r < 1$ corresponds to combined bending–torsion. The values of the r parameter and stress ratios (R) considered in the fatigue campaign are summarised in Table 1.

For the 10HNAP steel specimens, shown in Fig. 3(a), stationary and ergodic random loadings were applied considering a normal probability distribution with wideband frequency spectra in the range 0 to 60 Hz. In the case of bending–torsion, the r parameter was 0.5, i.e. the ratio of

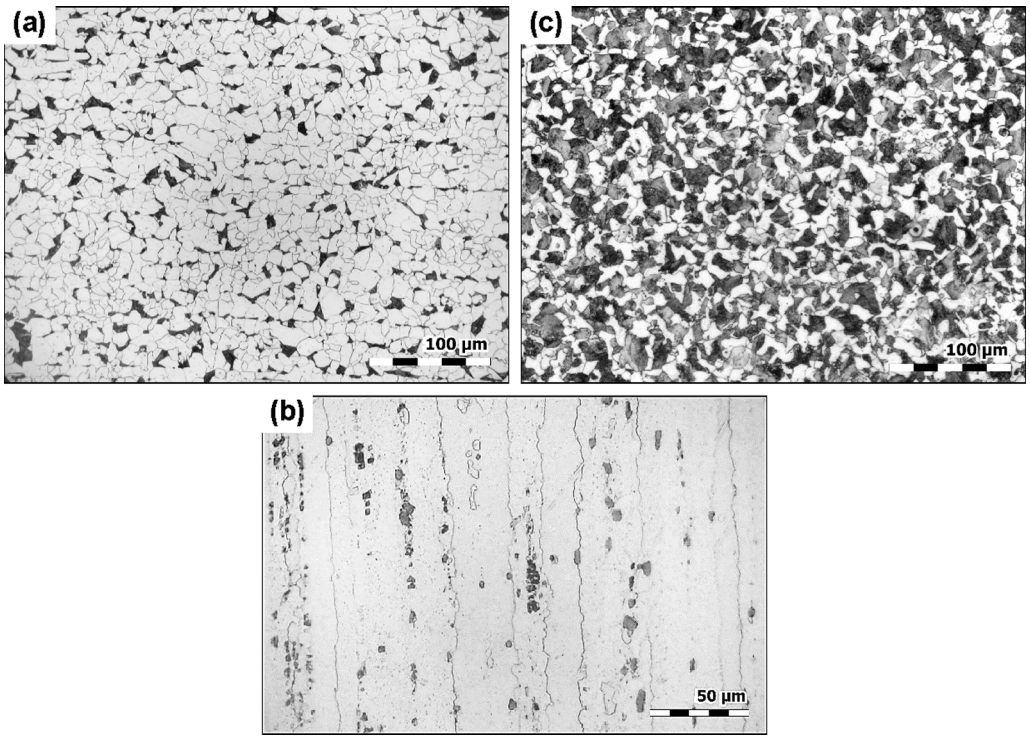

Fig. 2. Optical micrograph showing the microstructure: (a) 10HNAP steel (200x), (b) 2017A aluminium alloy (500x), and (c) S355J2 steel (200x).

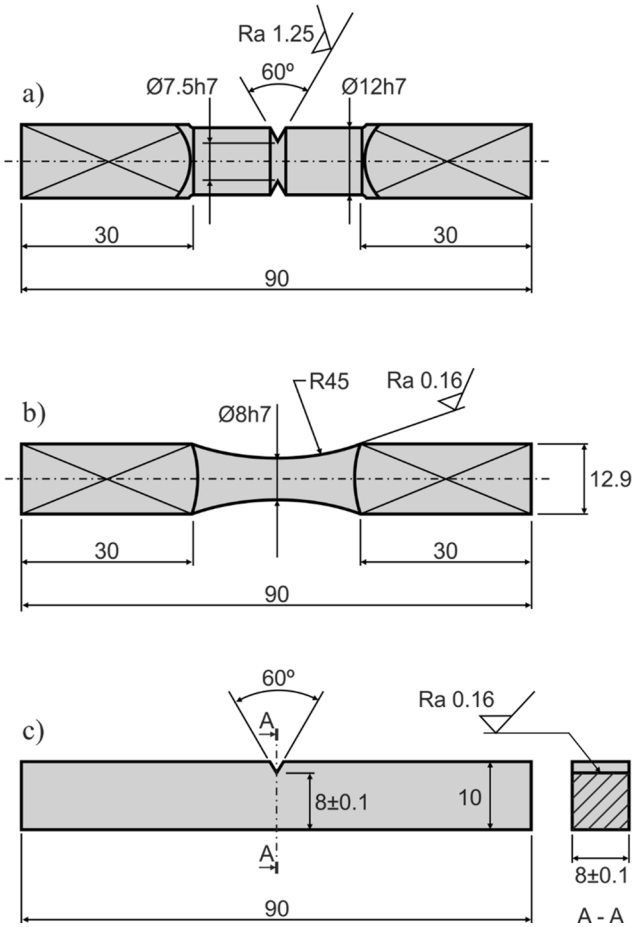

Fig. 3. Specimen geometries used in this study: (a) 10HNAP steel, (b) S355J2 steel, and (c) 2017-T4 aluminium alloy (units: mm).

normal stress amplitude to shear stress amplitude (σ_a/τ_a) was 1. More details about these tests can be found in a report by Achtelik [52].

Regarding the S355J2 steel specimens, shown in Fig. 3(b), fatigue tests were carried out under constant-amplitude loading. In the case of combined bending–torsion, tests were performed under nonproportional loading considering the values of the *r* parameter in the interval 0.16–0.6. A detailed description of these fatigue tests and the applied loading histories can be found in a report by Marciniak [50].

With respect to the 2017-T4 aluminium alloy specimens, as shown in Fig. 3(c), tests were also performed under constant-amplitude. For the bending–torsion cases, the values of the *r* parameter were in the range of 0.18–0.44, and the stress ratios were − 1, 0.5, and 0. Detailed information about these tests can be found in a report by Faszynka [53].

2.4. Fracture surface investigation

The fracture surfaces were examined using an optical three-dimensional noncontact focus-variation microscope. The InfiniteFocus G4 (see Fig. 5) made by Alicona combines both the small depth of focus of an optical microscope and vertical scanning to receive topographical and colour information [11,48]. In this study, the total fatigue fracture surfaces obtained for all tests were examined at a magnification of 10 times. Due to the reduced field view of the used microscope, the entire fracture area was mapped by combining nine rows and seven columns of data. Apart from the examination of the entire area, detailed analysis of specific regions of the specimens (e.g. initiation sites, propagation regions, and rupture areas) was performed at a magnification of 100 times.

The vertical and lateral nominal resolutions of every individual measurement was 79.3 nm and 3.91 µm, respectively. Generated real 3D surface images were processed using MountainsMap software produced by Digital Surf. The analysis of fracture surfaces was conducted in relative cartesian coordinates from the lowest point measured in the z-axis direction by default. Nonmeasured points, which are characteristic of the selected approach, were filled by a smooth shape determined from the neighbours. The total fracture area was chosen for the imaging. The three-dimensional parameters used in this study were computed for the

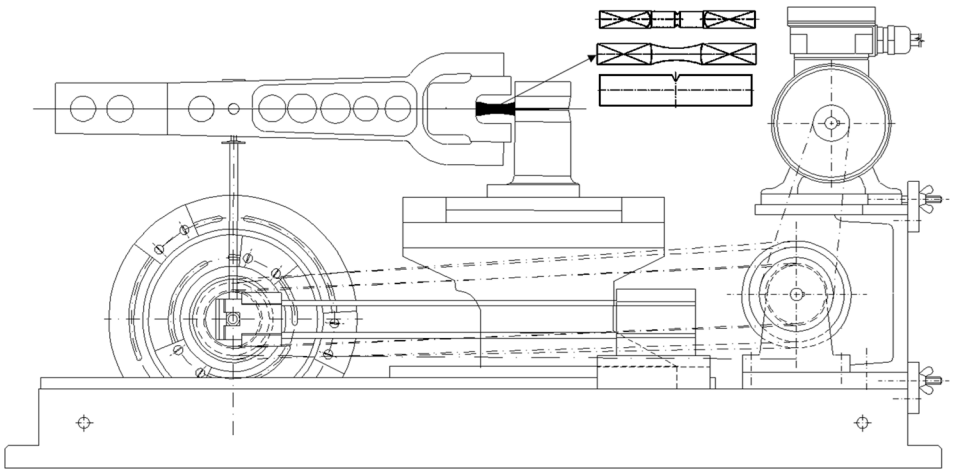

Fig. 4. MZGS-100 fatigue test stand used in this study.

Table 1
Loading parameters considered in the fatigue tests.

Material	$r = \frac{\tau_{max}}{\sigma_{max} + \tau_{max}}$	$R = \frac{\sigma_{min}}{\sigma_{max}}$	Reference
10HNAP	0; 0.5; 1	−1	[52]
S355J2	0; 0.16–0.6; 1	−1	[50]
2017-T4	0; 0.18–0.44; 1	−1; −0.5; 0	[53]

entire studied surfaces. In this study, 99 specimens were investigated — 30 for the 10HNAP steel, 50 for the S355J2 steel, and 19 for the 2017-T4 aluminium alloy — representing 30, 51, and 19%, respectively, of the investigated samples.

2.5. Proposed methodology

The main goal of the proposed methodology is the development of a fractal dimension based on the analysis of the entire area of the fracture surfaces caused by bending–torsion fatigue. This unifying approach, which is sensitive to different engineering materials and loading cases, makes possible the definition of quantitative relationships between the fatigue damage and statistical characteristics of pit and valley distributions. Furthermore, this systematic study makes it possible to estimate the causes of fatigue failure by accounting for its characteristics by means of fracture surface topography analysis.

Initially, the strategy consisted of obtaining uniform dimensions for the specimens. Thus, the current fracture surface was reduced by eliminating the final break region and the regions associated with the geometric discontinuities. In the case of circular cross sections (see Fig. 3 (a) and Fig. (b)), surface areas were reduced to circles with diameters of 7.2 and 7.8 mm, respectively. In the other case, as shown in Fig. 3(c), the surface areas were reduced to a rectangle of 7.2 × 7.5 mm. As an example, Fig. 6(a)–(c) show the initial and final surface areas utilised in this study for bending, bending–torsion, and torsion loadings, respectively. Overall, the pseudocolour views show significant differences associated with both the loading type and the geometric features.

In the second stage, the fractal dimension was calculated for all specimens from the final fracture surface areas. The fractal dimension makes it possible to use fractional geometric dimensions. A surface with a smaller fractal dimension is less complex and closer to a plane than a surface with a higher value, which is closer to a volume. In general, the fractal dimension varies between two and three for real surfaces. Here, the enclosing boxes method (EBM) introduced by Talu et al. [54] was used to determine the fractal dimension. The EBM divides the profile into smaller sections with a width ε and calculates the field Aε of all fields covering the entire profile [55,56]. This is an iterative procedure in which the width of the field is changed to create a graph, ln (Aε)/ln (ε). The fractal dimension, as shown in Fig. 7, was determined by computing the slope of the regression line for the entire fracture area. Surfaces were analyzed in relative coordinates (X, Y, and Z axes) with the Z axis, which coincided with the specimen axis, in heights from the lowest point by default. No additional filters were used. The EBM also does not filter noise, it is just an evaluation of the developed area at

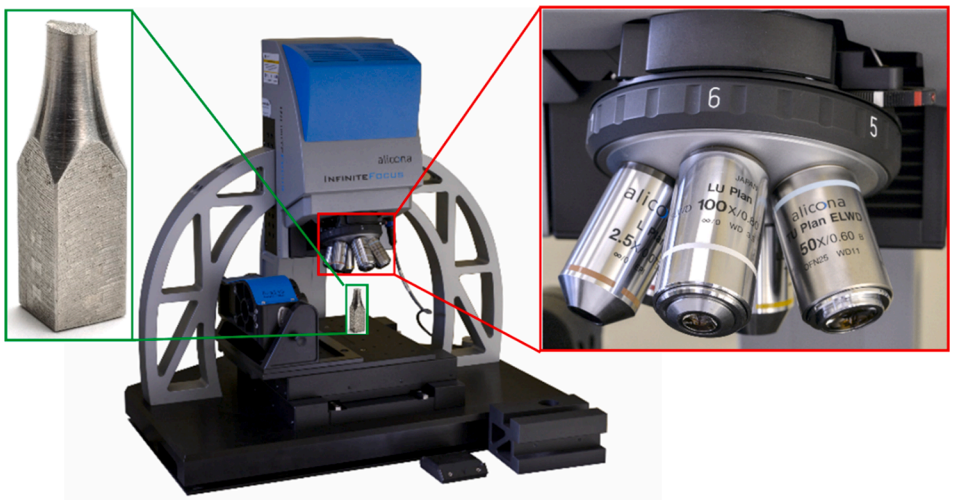

Fig. 5. Overview of the InfiniteFocus G4 measurement setup used in the study.

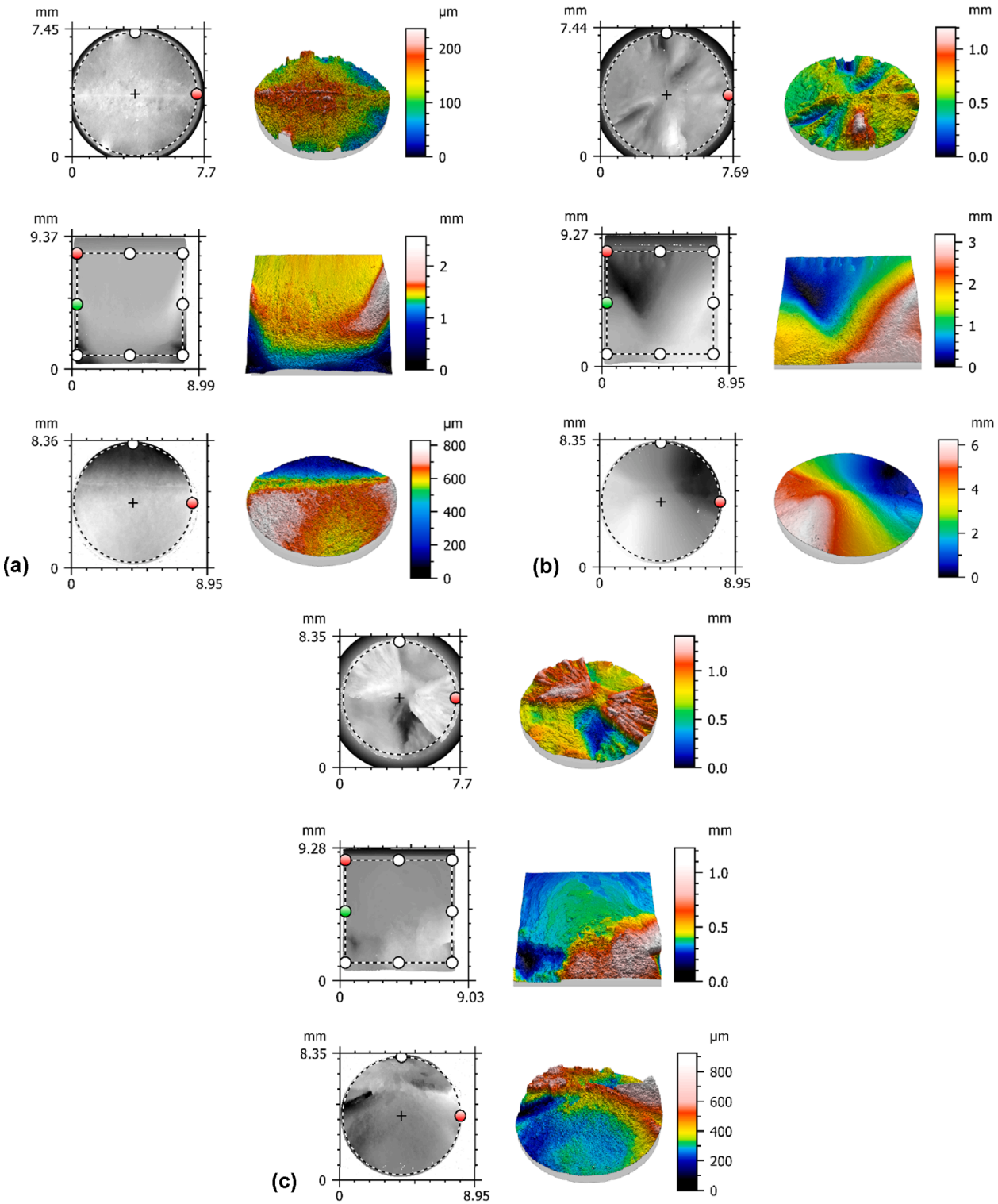

Fig. 6. Example of initial and final fracture surface areas utilised in this study: (a) bending, (b) bending–torsion, and (c) torsion loading — for each loading case, materials follow the order 10HNAP steel at the top, 2017-T4 aluminium alloy in the middle, and S355J2 steel at the bottom.

various scales, each point in the graph corresponds to one scale.

3. Results and discussion

3.1. Individual fracture zones

Fig. 8 shows three examples of the typical fracture surfaces obtained for the three materials under bending loading. The upper grey views are the original photographs taken by the measurement system after all the images of the fatigue fracture surface have been assembled, whereas the lower parts are the 3D views of the areas near the initiation sites. Maximum stresses occur at the specimen surface, making these points potential locations for fatigue crack initiation [57].

Under a fatigue bending load, the crack initiation sites of the 10HNAP steel specimens occur at the top and bottom of the circumferential notch. This leads to symmetrical propagation regions, whereas the

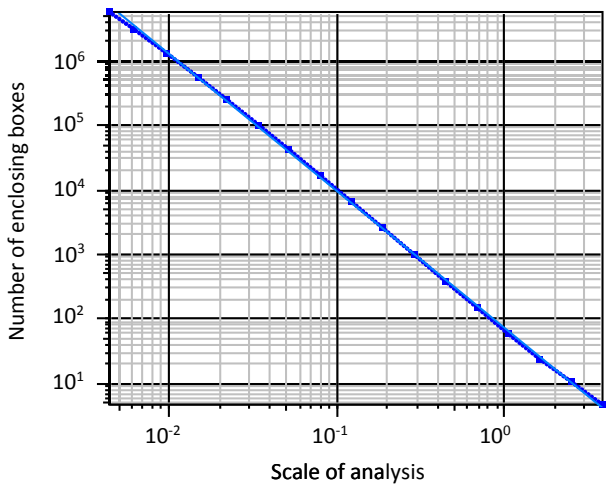

Fig. 7. Fractal analysis for the extracted area using the entire fracture method.

rupture area is located at the centre of the fracture surface. Regarding the 2017-T4 aluminium alloy specimens, as in Fig. 8(b), because of the geometric features associated with this specimen, the three zones are quite different from the previous case, i.e. only a single crack initiates at the notch, and then it propagates to the centre of the specimen, where one can see several crack fronts marked on the fracture surface. The rupture region can be distinguished at the top of the figure. In the case of Fig. 8(c), and similar to the 10HNAP steel specimens, the initiation sites of the S355J2 specification occur at the surface on the two opposite sides. This also leads to nearly symmetrical propagation zones, and the rupture zone occurs in the central part of the fracture surface.

Fig. 9 presents the fracture surfaces of selected areas of the S355J2 steel specimens under bending and bending–torsion. The figures on the left present the propagation areas, while the figures on the right show the rupture areas. The differences in the granularity and asperity of the fracture planes can be observed on the surfaces. For specimens subjected to pure bending, the propagation and rupture zones are characterised by a fine-grained structure. Nevertheless, for specimens under combined bending–torsion loading, the two above-mentioned zones exhibit important differences either in terms of in grain texture, or in terms of their directionality, which is associated with the existence of elongated grains. In contrast, this directional effect is attenuated in the rupture zone.

The results suggest that there are significant differences in the fatigue crack front developments, which affects the fracture surface features. From a fatigue point of view, these differences can be explained not only by the notch effect and the loading scenario but also by the yielding condition. Regardless of the specimen geometry, yielding at the initial fatigue stage is limited to a rather small area near the surface. In contrast, as the crack propagates, fatigue crack growth rates increase rapidly, leading to large yielding areas. In the case of notched configurations, at the early stage of crack growth, notch effects are likely to govern the initiation process, and the early stage of crack growth, by changing locally the yielding condition. Nevertheless, as the crack extends, this effect gradually disappears, and the yielding condition tends to be generalised throughout the entire crack front, which can explain the similarity of the fracture surface parameters. Thus, it was decided to analyse data from all fracture surfaces, and the fractal dimension Df was chosen to describe the topography.

3.2. Fractal dimension

Fig. 10 plot the fractal dimension values against the *r* parameter for 10HNAP steel, 2017-T4 aluminium alloy, and S355J2 steel specimens sequentially from the left, respectively. A table containing the full set of data presented in the graphs is shown in Appendix A (see Table A1). It is clear from the figure that fractal dimension values change in a relatively wide range, even for the case of pure bending and for the case of pure torsion. These changes of fractal dimension can be associated with crystal anisotropy. Such a mechanism occurs in single-crystal materials; therefore, it is reasonable to suppose a similar behaviour in polycrystalline materials.

A wider analysis of Fig. 10 reveals that fractal dimension values tend to be higher for pure bending than for pure torsion and that the values

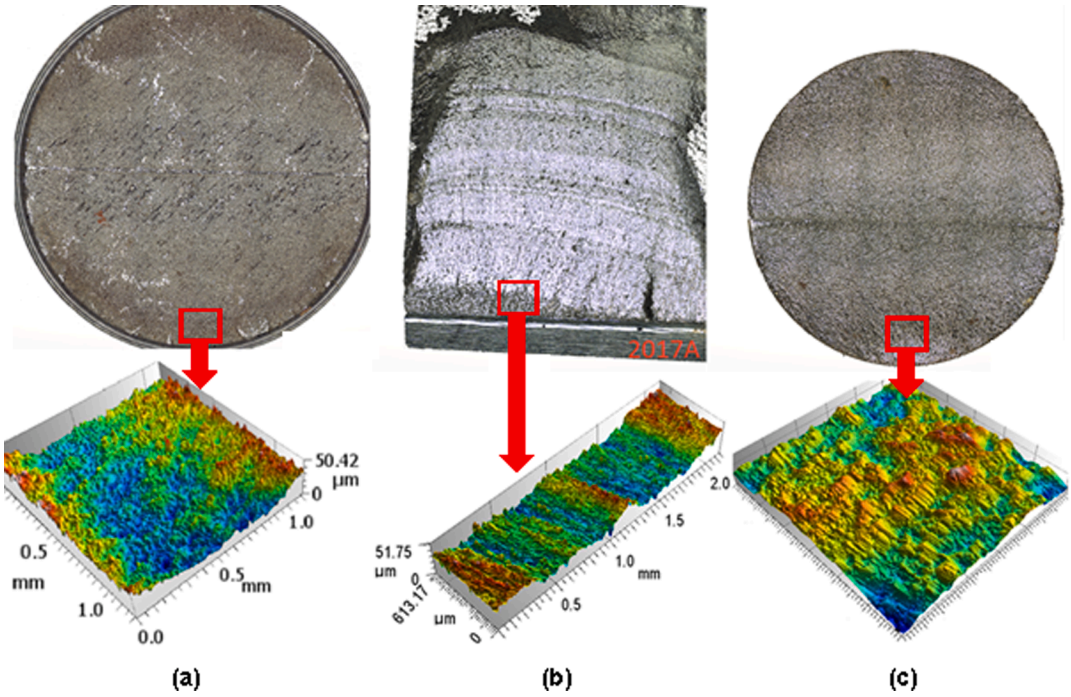

Fig. 8. Examples of fracture surfaces resulting from bending loads with marked areas of fatigue crack initiation for the three types of specimens: a) 10HNAP steel, (b) 2017-T4 aluminium alloy, and (c) S355J2 steel.

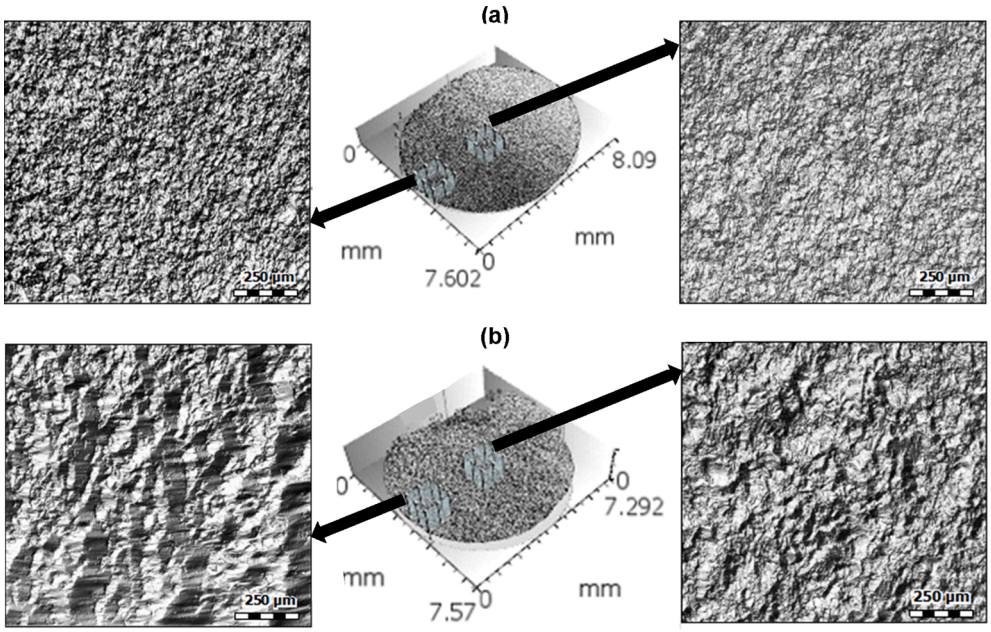

Fig. 9. Selected S355J2 steel specimen showing the propagation and rupture areas for (a) bending ($\sigma_{max} = 475$ MPa) and (b) combined bending–torsion ($\sigma_{max} = 420$ MPa, and $\tau_{max} = 90$ MPa) loading.

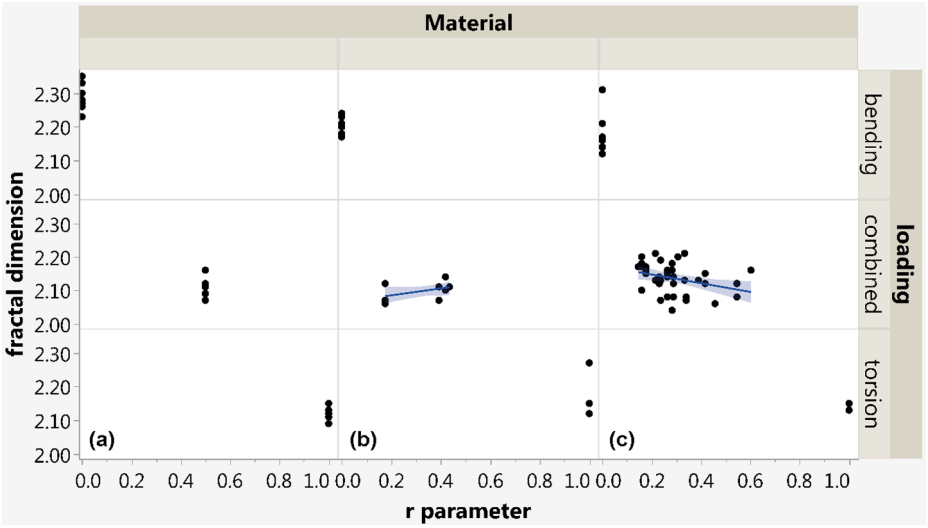

Fig. 10. Fractal dimension versus *r* parameter for the studied materials and the applied loading scenarios: (a) 10HNAP steel, (b) 2017-T4 aluminium alloy, and (c) S355J2 steel.

for combined bending–torsion are the lowest. It is also clear that the correlation between the fractal dimension and the *r* parameter is ambiguous. For the 2017-T4 aluminium alloy, the trend is reversed, and the fractal dimension values increase. With respect to the 10HNAP steel, the fractal dimensions increase with decreasing *r* values. Under bending–torsion, when the *r* parameter is 0.5, the fractal dimension values change in the range of 2.07–2.16.

To identify the dependencies between the fractal dimension and the *r* parameter, the results for each investigated material were fitted using quadratic curves in the following form.

$$Df = A + B \bullet \mathrm{r} + \mathrm{C} \bullet \mathrm{r}^2 \tag{2}$$

where A, B, and C are unknowns. The fitted functions are plotted in Fig. 11(a)–(c) for the 10HNAP steel, 2017-T4 aluminium alloy, and S355J2 steels, respectively. Overall, one can see that the fractal dimension changes randomly with the parameter *r* in the three cases. In the three cases, but particularly for the S355J2 steel, it is difficult to observe a strong correlation between the r parameter and the fractal dimension.

The estimated coefficients of the quadratic curves and several statistical variables associated with the constants are presented in Table 2 for the 10HNAP steel, 2017-T4 aluminium alloy, and S355J2 steel. Table 3 compiles a number of other statistical parameters computed to evaluate the quality of results: the Akaike information criterion (AIC), which is an estimator of the out-of-sample prediction error; the Bayesian information criterion (BIC), which generally penalises free parameters more strongly than the AIC, the sum of squares of the residual error (SSE), which measures the overall difference between data and the values predicted by the estimation model, the mean squared error (MSE), which is a risk function corresponding to the expected value of the squared error loss; the root mean square error (RMSE), which is the square root of the average of squared errors; and the coefficient of

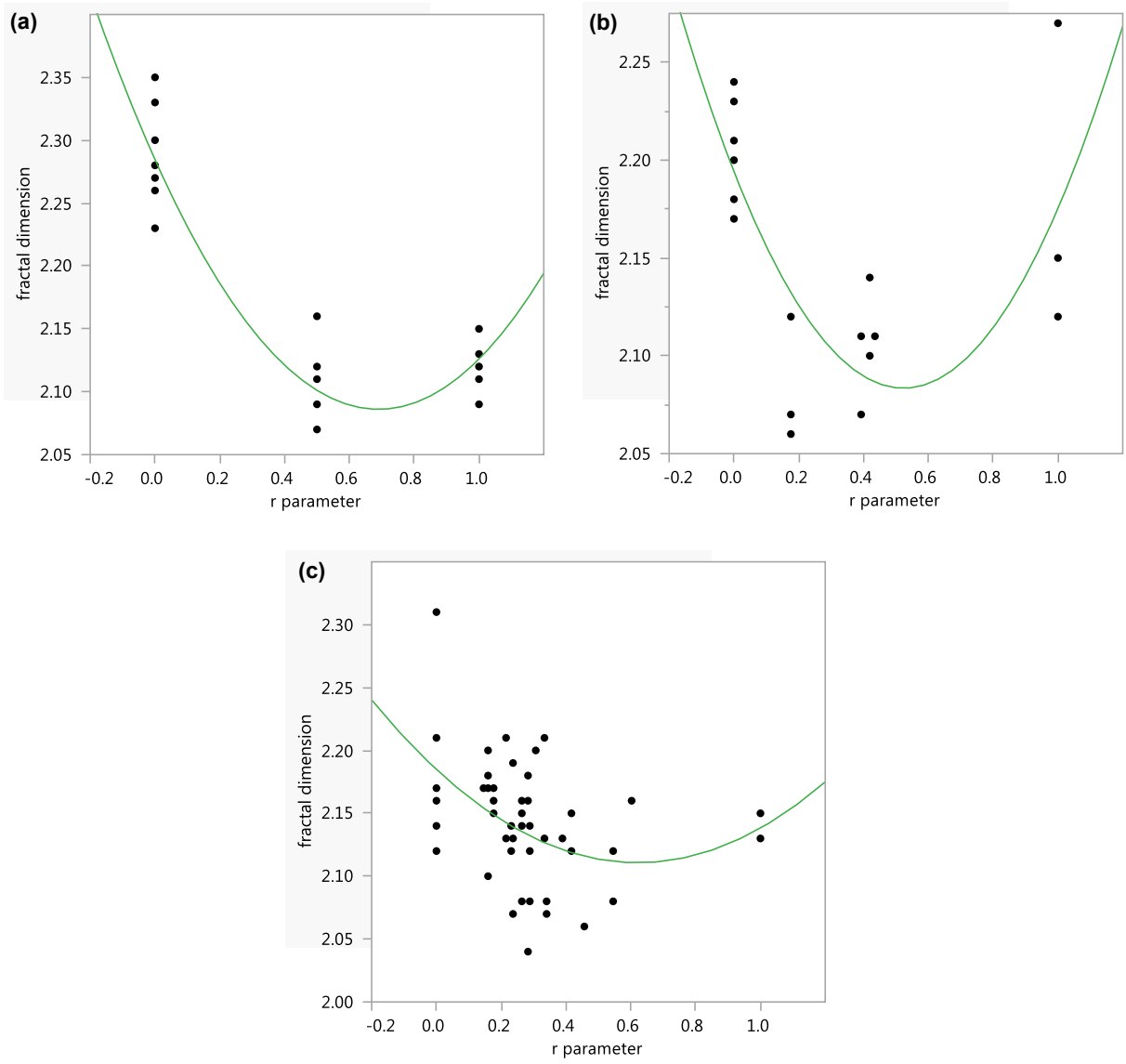

Fig. 11. Fitted curve for (a) 10HNAP steel, (b) 2017-T4 aluminium alloy, and (c) S355J2 steel.

Table 2
Estimated coefficients and their statistical values for the studied materials.

Material	Parameter	Estimate	Std Error	Wald Chi-Square	Prob > Chi-Square
10HNAP	A	2.285×10^{0}	8.165×10^{-3}	7.828×10^{4}	$<1 \times 10^{-4}$ *
	B	-5.752×10^{-1}	4.447×10^{-2}	1.673×10^{2}	$<1 \times 10^{-4}$ *
	C	4.166×10^{-1}	4.317×10^{-2}	9.314×10^{1}	$<1 \times 10^{-4}$ *
2017-T4	A	2.194×10^{0}	1.609×10^{-2}	1.860×10^{4}	$<1 \times 10^{-4}$ *
	B	-4.232×10^{-1}	9.932×10^{-2}	1.815×10^{1}	$<1 \times 10^{-4}$ *
	C	4.043×10^{-1}	9.572×10^{-2}	1.784×10^{1}	$<1 \times 10^{-4}$ *
S355J2	A	2.185×10^{0}	1.296×10^{-2}	2.841×10^{4}	$<1 \times 10^{-4}$ *
	B	-2.386×10^{-1}	7.063×10^{-2}	1.142×10^{1}	7×10^{-4} *
	C	1.920×10^{-1}	7.590×10^{-2}	6.401×10^{0}	1×10^{-2} *

Table 3
Statistical values of the quadratic curve for the studied materials.

Material	AIC	BIC	SSE	MSE	RMSE	R-Square
10HNAP	-1.250×10^{2}	-1.210×10^{2}	1.980×10^{-2}	7.334×10^{-4}	2.708×10^{-2}	9.119×10^{-1}
2017-T4	-5.700×10^{1}	5.608×10^{1}	3.128×10^{-2}	1.955×10^{-3}	4.421×10^{-2}	5.344×10^{-1}
S355J2	-1.663×10^{2}	-1.595×10^{2}	8.815×10^{-2}	1.875×10^{-3}	4.331×10^{-2}	2.206×10^{-1}

determination (R-square), which is commonly used to represent the proportion of the variance for a dependent variable that is explained by an independent variable or variables in a regression model.

Based on the statistical values presented in Tables 2 and 3, one can conclude that the estimated quadratic curves for the 10HNAP steel and the 2017-T4 aluminium alloy provide good fitting results, i.e. a valid relationship between the fractal dimension and the applied load; therefore, they can be used to correlate the fractal dimension with the *r* parameter. However, for the S355J2 steel, the statistical values suggest that the curve regression in this case yields unsatisfactory results. A

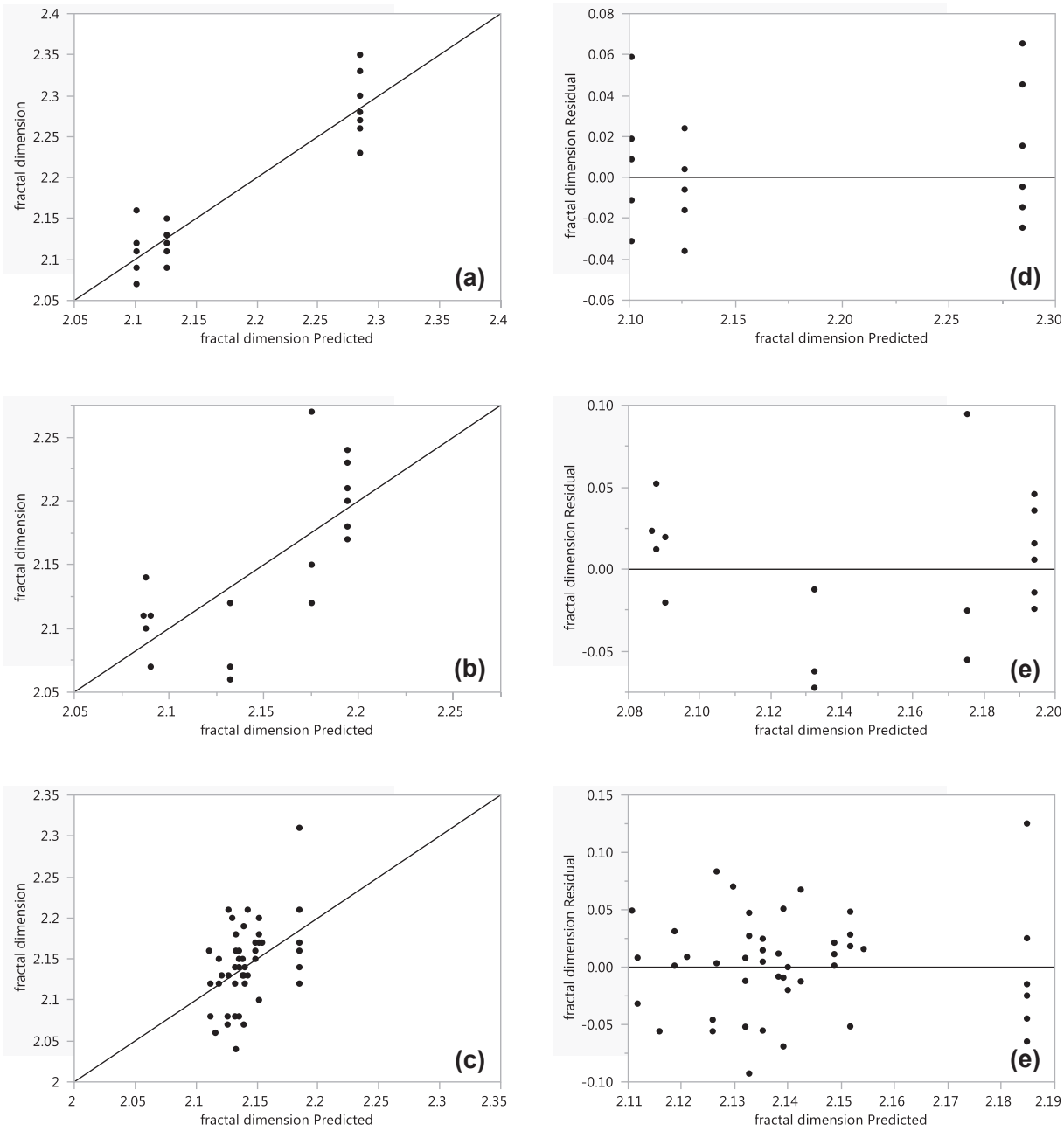

Fig. 12. Experimental fractal dimensions versus calculated fractal dimensions for the studied materials under bending–torsion and torsion (a,b,c), and the corresponding fractal dimension residuals (d,e,f).

comparison between the predicted and measured fractal dimensions is plotted in Fig. 12 for the three tested materials under combined bending–torsion and torsion loadings. For comparability, fractal dimension residuals are also plotted. In the case of Fig. 12(a), the values of the fractal dimension are in the range of 2.07 to 2.35, and the residuals vary by ± 0.06, which corresponds to a maximum difference of approximately 21%. As shown in Fig. 12(b), the maximum differences are slightly higher, approximately 36%, which results from a residual of approximately ± 0.75 and a fractal dimension within the interval of 2.06 to 2.27. In the case of the S355J2 steel, the maximum differences are similar to those of the 2017-T4 aluminium alloy, approximately 37%, i.e. a fractal dimension that varies in the interval 2.04 to 2.31, and residuals in the range of ± 0.1.

For all analysed samples, the vertexes of the fitted parabolas (see Fig. 11) corresponded to values of the *r* parameter approximately 0.7, 0.5, and 0.6 for the 10HNAP steel, 2017-T4 aluminium alloy, and S355J2 steel, respectively. The axis of symmetry of these functions means that when an attempt is made to estimate the method of load causing damage from the fractal dimension, there is a risk of incorrect interpretation. Because there is a plane curve that is mirror-symmetrical and is approximately U-shaped, especially in the case of the 2017-T4 aluminium alloy, Df values are similar either for pure bending or for pure torsion. The largest asymmetry between the two above-mentioned loading modes occurred for the circumferential notched 10HNAP specimens. To visualise this, average values (see the × markers), median values and 25th and 75th percentiles (see the blue rectangles), and the most extreme data points (see the whiskers) of Df are displayed in Fig. 13 at appropriate load levels for the three studied materials.

Table 4 summarises the values of the averaged fractal dimension for different loading cases examined in this study. Regarding the maximum (Df_{max}) and minimum (Df_{min}) values of the fractal dimension, regardless of the tested material, a fixed relationship was found with the

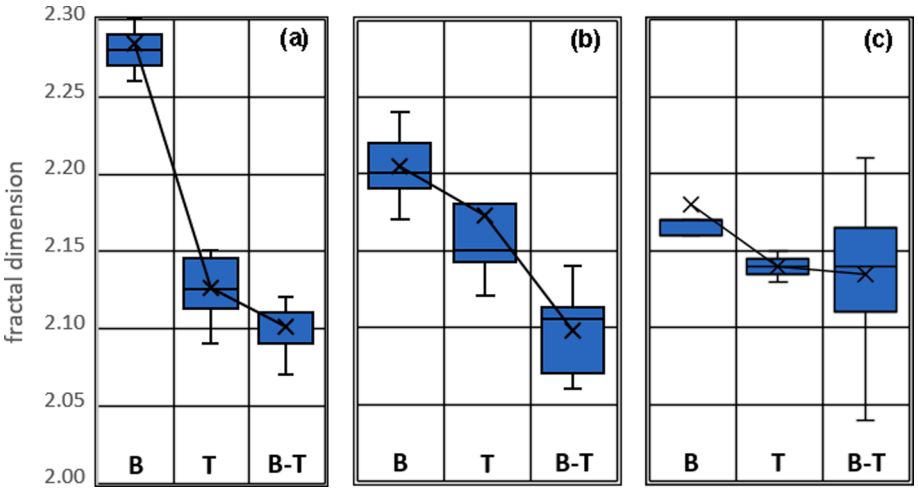

Fig. 13. Specimen fracture surfaces averaged values for fractal dimension Df: (a) 10HNAP steel, (b) 2017-T4 aluminium alloy, and (c) S355J2 steel.

Table 4
Averaged fractal dimension for bending, torsion, and bending–torsion loadings.

Loading type	10HNAP	2017-T4	S355J2
Bending	2.28	2.20	2.18
Torsion	2.13	2.17	2.14
Bending–Torsion	2.10	2.10	2.13

investigated loading scenarios, i.e. Df_{max} occurred for bending, while Df_{min} occurred for combined bending–torsion. Thus, the fractal dimension of the extreme values can also be used in the failure analysis, which is an interesting outcome. As an example, Fig. 14 shows the fracture surfaces and corresponding graphs of the extreme values of the fractal dimension for the 10HNAP steel. The scale of analysis takes similar values (>1 mm) for the samples with the minimum value of fractal dimension (Df_{min} = 2.07, for bending–torsion loading) and the maximum value of fractal dimension (Df_{max} = 2.35, for bending loading). Moreover, the number of enclosing boxes is different, i.e.

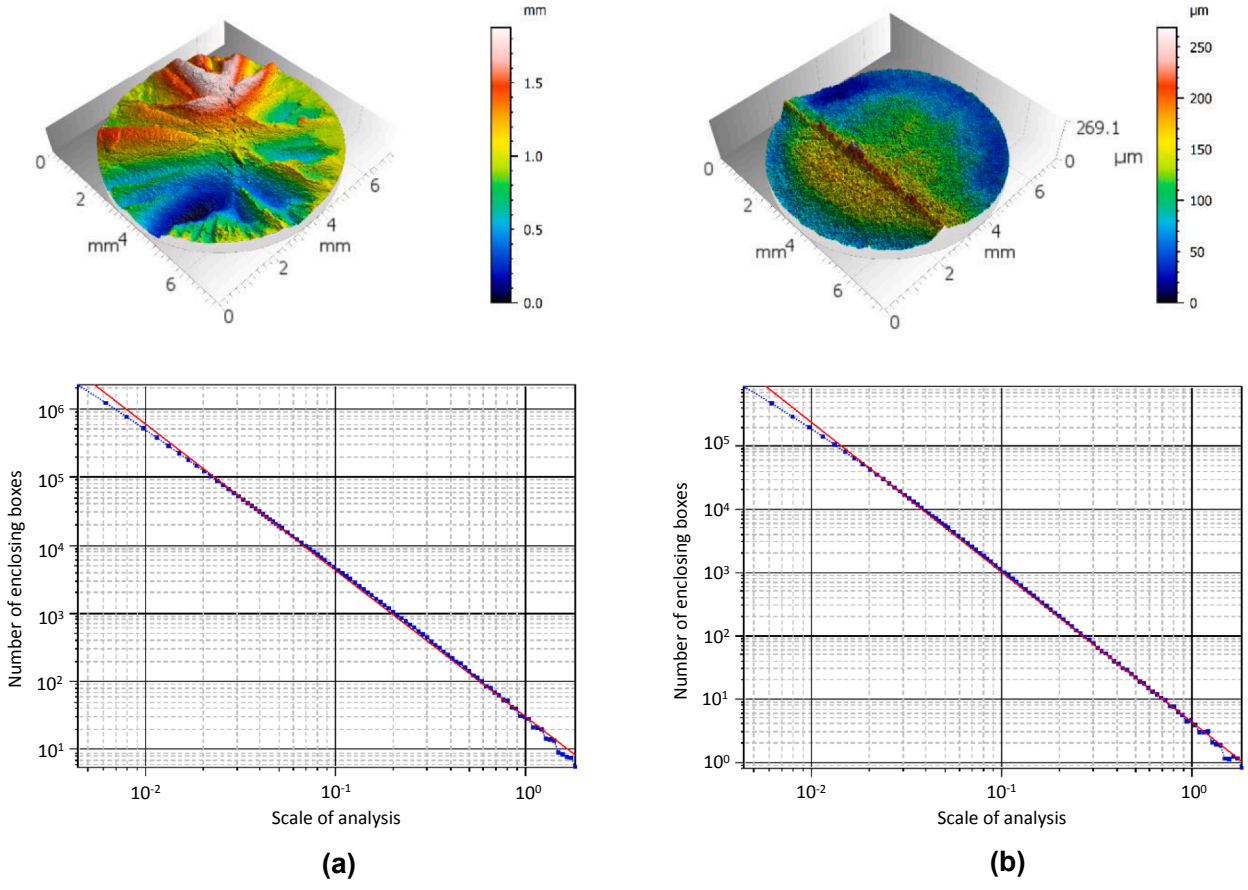

Fig. 14. Fractal dimension based on the extreme values determined by the EBM for the 10HNAP steel: (a) minimum Df value (2.07) and (b) maximum Df value (2.35).

higher than 10^6 for the minimum value of Df and lower than 10^6 for the maximum value of Df. The coefficients of correlation (R-square) of linear fits (red line) were 0.9987 and 0.9991, indicating that the data were excellently fitted by linear functions. In summary, this means that the fractal dimension, supported by other parameters of quantitative fractography, can be an effective tool for complete failure analysis.

4. Conclusions

The relationship between the fracture surface topography and fatigue loading scenario was investigated systematically using fractal dimension concepts and the total fracture surface area method. In this study, three different engineering materials (an aluminium alloy, a construction steel, and a structural steel), three different geometries (circumferential V-notches, lateral V-notches, and smooth specimens), and three types of loading (pure bending, pure torsion, and combined bending–torsion) were investigated. One of the main outcomes is the development of a fractal-based approach to estimate the effect of the loading rate under biaxial fatigue loading after failure. The following conclusions can be drawn.

- Fatigue crack initiation and fatigue crack growth were greatly different for the different cases, which was explained by the combination of both the loading type and geometrical features of the tested geometries.
- The fractal dimension changed over a relatively wide range for the different loading cases: pure bending, pure torsion, and combined bending–torsion. These differences were explained by the crystal anisotropy.
- A comparison between the predicted and measured fractal values shows that it is possible to establish valid relationships between the fractal dimension and applied fatigue loading.
- The average value of the fractal dimension, regardless of the tested material, was higher for bending than for torsion and combined bending–torsion, which indicates a higher sensitivity of the Df parameter to the first loading type.
- The fractal dimension residuals were ± 0.06, ±0.75, and ± 0.1 for the 10HNAP steel, 2017-T4 aluminium alloy, and S355J2 steel, corresponding to differences of 21, 36, and 37%, respectively.
- The maximum and minimum fractal values, regardless of the tested material, exhibited a fixed behaviour: the maximum values were found for bending, while the minimum values were found for bending–torsion.
- An analysis of the fractal dimension based on the extreme values (i.e. maximum and minimum values) led to high R-square correlations, ranging from 0.9987 to 0.9991, demonstrating that the data can be fitted using linear functions.

The main goal of this paper was to correlate the fatigue damage with fractal dimension concepts, and it opens interesting avenues for further investigation. To create a wider picture and a stronger understanding of the interdependencies between the fractal dimension and fatigue damage, future research is planned in order to focus on other engineering materials and loading scenarios, including additively manufactured metals, to identify valid links not only between the loading history and the fractal dimension but also with other fractographic parameters in order to develop an effective tool for complete failure analysis.

CRediT authorship contribution statement

Wojciech Macek: Conceptualization, Methodology, Software, Formal analysis, Data curation, Investigation, Writing – original draft, Visualization, Supervision. **Ricardo Branco:** Validation, Formal analysis, Writing - review & editing, Supervision. **Mateusz Korpyś:** Software, Writing - review & editing. **Tadeusz Łagoda:** Resources, Supervision.

Declaration of Competing Interest

The authors declare that they have no known competing financial interests or personal relationships that could have appeared to influence the work reported in this paper.

Acknowledgments:

This research is sponsored by FEDER funds through the program COMPETE – Programa Operacional Factores de Competitividade – and by national funds through FCT – Fundação para a Ciência e a Tecnologia – under the project UIDB/00285/2020.

Appendix A

(see table A1)

Table A1
Fractal dimension versus r parameter for the studied materials.

S355J2 steel		2017-T4 aluminium alloy		10HNAP steel	
r parameter	Fractal dimension	r parameter	Fractal dimension	r parameter	Fractal dimension
0.000	2.16	0.000	2.18	0.000	2.28
0.000	2.21	0.000	2.20	0.000	2.27
0.000	2.31	0.000	2.23	0.000	2.23
0.000	2.17	0.000	2.21	0.000	2.27
0.000	2.12	0.000	2.17	0.000	2.28
0.000	2.17	0.000	2.20	0.000	2.28
0.000	2.14	0.000	2.24	0.000	2.33
0.000	2.17	0.176	2.06	0.000	2.26
0.000	2.17	0.176	2.07	0.000	2.28
0.145	2.17	0.176	2.12	0.000	2.35
0.159	2.10	0.393	2.07	0.000	2.30
0.159	2.20	0.393	2.11	0.500	2.09
0.159	2.17	0.419	2.14	0.500	2.12
0.159	2.18	0.419	2.10	0.500	2.09
0.176	2.17	0.435	2.11	0.500	2.11
0.176	2.16	1.000	2.27	0.500	2.09
0.176	2.15	1.000	2.15	0.500	2.09
0.215	2.13	1.000	2.12	0.500	2.16
0.215	2.13	1.000	2.15	0.500	2.09
0.215	2.21			0.500	2.07
0.231	2.12			1.000	2.13
0.231	2.14			1.000	2.11
0.236	2.19			1.000	2.12
0.236	2.07			1.000	2.15
0.236	2.13			1.000	2.15
0.264	2.08			1.000	2.09
0.264	2.15			1.000	2.11
0.264	2.16			1.000	2.12
0.264	2.14			1.000	2.15
0.283	2.16			1.000	2.13
0.283	2.04				
0.283	2.18				
0.288	2.12				
0.288	2.08				
0.288	2.14				
0.307	2.20				
0.333	2.13				
0.333	2.21				
0.340	2.07				
0.340	2.08				
0.389	2.13				
0.417	2.12				
0.417	2.15				
0.457	2.06				
0.545	2.08				
0.545	2.08				
0.545	2.12				
0.602	2.16				
1.000	2.15				
1.000	2.13				

References

[1] M. Szala, K. Beer-Lech, M. Walczak, A study on the corrosion of stainless steel floor drains in an indoor swimming pool, Eng. Fail. Anal. 77 (2017) 31–38, https://doi.org/10.1016/j.engfailanal.2017.02.014.

[2] R. Branco, J. Costa, F. Berto, S. Razavi, J. Ferreira, C. Capela, L. Santos, F. Antunes, Low-cycle fatigue behaviour of AISI 18Ni300 maraging steel produced by selective laser melting, Metals (Basel). 8 (1) (2018) 32, https://doi.org/10.3390/met8010032.

[3] T.M. Mower, M.J. Long, Mechanical behavior of additive manufactured, powder-bed laser-fused materials, Mater. Sci. Eng. A. 651 (2016) 198–213, https://doi.org/10.1016/j.msea.2015.10.068.

[4] B. Yang, M. Wu, X. Li, J. Zhang, H. Wang, Effects of cold working and corrosion on fatigue properties and fracture behaviors of precipitate strengthened Cu-Ni-Si alloy, Int. J. Fatigue. 116 (2018) 118–127, https://doi.org/10.1016/J.IJFATIGUE.2018.06.017.

[5] B. Wisner, A. Kontsos, Investigation of particle fracture during fatigue of aluminum 2024, Int. J. Fatigue. 111 (2018) 33–43, https://doi.org/10.1016/J.IJFATIGUE.2018.02.001.

[6] T. Kobayashi, D.A. Shockey, The relationship between fracture surface roughness and fatigue load parameters, Int. J. Fatigue. 23 (2001) 135–142, https://doi.org/10.1016/S0142-1123(01)00149-9.

[7] L. Molent, A. Spagnoli, A. Carpinteri, R. Jones, Using the lead crack concept and fractal geometry for fatigue lifing of metallic structural components, Int. J. Fatigue. 102 (2017) 214–220, https://doi.org/10.1016/J.IJFATIGUE.2017.04.001.

[8] K.F. Walker, J.M. Lourenço, S. Sun, M. Brandt, C.H. Wang, Quantitative fractography and modelling of fatigue crack propagation in high strength AerMet®100 steel repaired with a laser cladding process, Int. J. Fatigue. 94 (2017) 288–301, https://doi.org/10.1016/J.IJFATIGUE.2016.06.031.

[9] T.G. Mathia, P. Pawlus, M. Wieczorowski, Recent trends in surface metrology, Wear. 271 (3-4) (2011) 494–508, https://doi.org/10.1016/j.wear.2010.06.001.

[10] W. Grzesik, Prediction of the Functional Performance of Machined Components Based on Surface Topography: State of the Art, J. Mater. Eng. Perform. 25 (10) (2016) 4460–4468, https://doi.org/10.1007/s11665-016-2293-z.

[11] W. Kaplonek, K. Nadolny, Advanced 3D laser microscopy for measurements and analysis of vitrified bonded abrasive tools, J. Eng. Sci. Technol. (2012).

[12] E. Merson, V. Danilov, D. Merson, A. Vinogradov, Confocal laser scanning microscopy: The technique for quantitative fractographic analysis, Eng. Fract. Mech. 183 (2017) 147–158, https://doi.org/10.1016/j.engfracmech.2017.04.026.

[13] Q. Zhong, Z. Zhao, Z. Zhang, Development of “fractography” and research of fracture micromechanism, Jixie Qiangdu/Journal Mech. Strength. (2005).

[14] W. Macek, D. Rozumek, G.M. Królczyk, Surface topography analysis based on fatigue fractures obtained with bending of the 2017A–T4 alloy, Meas. J. Int. Meas. Confed. 152 (2020) 107347, https://doi.org/10.1016/j.measurement.2019.107347.

[15] P. Modrzyński, A. Olejniczak, A. Zięba, P. Kunicki, M. Tomanik, M. Wielebski, The influence of sub-wavelength effective refractive index layer on the transmittance of LYSO scintillatory, Acta Phys. Pol. A. 131 (6) (2017) 1565–1569, https://doi.org/10.12693/APhysPolA.131.1565.

[16] J. Polák, J. Man, Experimental evidence and physical models of fatigue crack initiation, Int. J. Fatigue. 91 (2016) 294–303, https://doi.org/10.1016/j.ijfatigue.2016.02.021.

[17] K. Rodak, A. Brzezińska, R. Molak, Compression with oscillatory torsion applied after solution treatment and aging treatment of CuCr0.6 alloy for grain refinement: Microstructure, mechanical and electrical properties, Mater. Sci. Eng. A. 724 (2018) 112–120, https://doi.org/10.1016/j.msea.2018.03.077.

[18] M. Soleimani, H. Mirzadeh, C. Dehghanian, Phase transformation mechanism and kinetics during step quenching of st37 low carbon steel, Mater. Res. Express. 6 (11) (2019) 1165f2, https://doi.org/10.1088/2053-1591/ab4960.

[19] M.B. Djukic, G.M. Bakic, V. Sijacki Zeravcic, A. Sedmak, B. Rajicic, The synergistic action and interplay of hydrogen embrittlement mechanisms in steels and iron: Localized plasticity and decohesion, Eng. Fract. Mech. 216 (2019) 106528, https://doi.org/10.1016/j.engfracmech.2019.106528.

[20] T.L. Burnett, R. Kelley, B. Winiarski, L. Contreras, M. Daly, A. Gholinia, M. G. Burke, P.J. Withers, Large volume serial section tomography by Xe Plasma FIB dual beam microscopy, Ultramicroscopy 161 (2016) 119–129, https://doi.org/10.1016/j.ultramic.2015.11.001.

[21] K. Fisher, E. Marquis, Comparing Plasma-FIB and Ga-FIB Preparation of Atom Probe Tomography Samples, Microsc. Microanal. 22 (S3) (2016) 692–693, https://doi.org/10.1017/S1431927616004311.

[22] B. Stępak, P. Dzienny, V. Franke, P. Kunicki, T. Gotszalk, A. Antończak, Femtosecond laser-induced ripple patterns for homogenous nanostructuring of pyrolytic carbon heart valve implant, Appl. Surf. Sci. 436 (2018) 682–689, https://doi.org/10.1016/j.apsusc.2017.12.016.

[23] X. Feng, N. Senin, R. Su, S. Ramasamy, R. Leach, Optical measurement of surface topographies with transparent coatings, Opt. Lasers Eng. 121 (2019) 261–270, https://doi.org/10.1016/J.OPTLASENG.2019.04.018.

[24] N. Senin, A. Thompson, R.K. Leach, Characterisation of the topography of metal additive surface features with different measurement technologies, Meas. Sci. Technol. 28 (9) (2017) 095003, https://doi.org/10.1088/1361-6501/aa7ce2.

[25] W.J. Stemp, D.A. Macdonald, M.A. Gleason, Testing imaging confocal microscopy, laser scanning confocal microscopy, and focus variation microscopy for microscale measurement of edge cross-sections and calculation of edge curvature on stone tools: Preliminary results, J. Archaeol. Sci. Rep. 24 (2019) 513–525, https://doi.org/10.1016/J.JASREP.2019.02.010.

[26] A. Townsend, N. Senin, L. Blunt, R.K. Leach, J.S. Taylor, Surface texture metrology for metal additive manufacturing: a review, Precis. Eng. 46 (2016) 34–47, https://doi.org/10.1016/j.precisioneng.2016.06.001.

[27] M. FONTE, F. ROMEIRO, M. FREITAS, Environment effects and surface roughness on fatigue crack growth at negative R-ratios, Int. J. Fatigue 29 (9-11) (2007) 1971–1977, https://doi.org/10.1016/j.ijfatigue.2007.02.027.

[28] W. Macek, R. Branco, J. Trembacz, J.D. Costa, J.A.M. Ferreira, C. Capela, Effect of multiaxial bending-torsion loading on fracture surface parameters in high-strength steels processed by conventional and additive manufacturing, Eng. Fail. Anal. 118 (2020) 104784, https://doi.org/10.1016/j.engfailanal.2020.104784.

[29] J. QUINN, G. QUINN, J. KELLY, S. SCHERRER, Fractographic analyses of three ceramic whole crown restoration failures, Dent. Mater. 21 (10) (2005) 920–929, https://doi.org/10.1016/j.dental.2005.01.006.

[30] H.M. Huang, C.M. Tsai, C.C. Chang, C.T. Lin, S.Y. Lee, Evaluation of loading conditions on fatigue-failed implants by fracture surface analysis, Int. J. Oral Maxillofac. Implants (2005), https://doi.org/10.1021/ol900433g.

[31] G.D. Quinn, NIST recommended practice guide : Gaithersburg, MD (2007), https://doi.org/10.6028/NBS.SP.960-16.

[32] K. Slámečka, J. Pokluda, M. Kianicová, Š. Major, I. Dvořák, Quantitative fractography of fish-eye crack formation under bending-torsion fatigue, Int. J. Fatigue 32 (6) (2010) 921–928, https://doi.org/10.1016/j.ijfatigue.2009.07.009.

[33] W. Macek, Fractal analysis of the bending-torsion fatigue fracture of aluminium alloy, Eng. Fail. Anal. 99 (2019) 97–107, https://doi.org/10.1016/j.engfailanal.2019.02.007.

[34] W. Macek, Post-failure fracture surface analysis of notched steel specimens after bending-torsion fatigue, Eng. Fail. Anal. 105 (2019) 1154–1171, https://doi.org/10.1016/j.engfailanal.2019.07.056.

[35] W. Macek, Z. Marciniak, R. Branco, D. Rozumek, G.M. Królczyk, A fractographic study exploring the fracture surface topography of S355J2 steel after pseudo-random bending-torsion fatigue tests, Measurement 178 (2021) 109443, https://doi.org/10.1016/j.measurement.2021.109443.

[36] B.B. Mandelbrot, The Fractal Geometry of Nature, 2nd ed., Times Books, New York, 1982.

[37] B.B. Mandelbrot, D.E. Passoja, A.J. Paullay, Fractal character of fracture surfaces of metals, Nature. 308 (5961) (1984) 721–722, https://doi.org/10.1038/308721a0.

[38] M.A. Issa, M.A. Issa, M.S. Islam, A. Chudnovsky, Fractal dimension-a measure of fracture roughness and toughness of concrete, Eng. Fract. Mech. 70 (1) (2003) 125–137, https://doi.org/10.1016/S0013-7944(02)00019-X.

[39] E. Charkaluk, M. Bigerelle, A. Iost, Fractals and fracture, Eng. Fract. Mech. 61 (1) (1998) 119–139, https://doi.org/10.1016/S0013-7944(98)00035-6.

[40] A. Carpinteri, B. Chiaia, P. Cornetti, A scale-invariant cohesive crack model for quasi-brittle materials, Eng. Fract. Mech. 69 (2) (2002) 207–217, https://doi.org/10.1016/S0013-7944(01)00085-6.

[41] P. Kotowski, Fractal dimension of metallic fracture surface, Int. J. Fract. 141 (1-2) (2006) 269–286, https://doi.org/10.1007/s10704-006-8264-x.

[42] S. Sahu, P.C. Yadav, S. Shekhar, Fractal Analysis as Applied to Fractography in Ferritic Stainless Steel, Metallogr. Microstruct. Anal. 6 (6) (2017) 598–609, https://doi.org/10.1007/s13632-017-0396-z.

[43] O. Hilders, N. Zambrano, The effect of aging on impact toughness and fracture surface fractal dimension in SAF 2507 super duplex stainless steel, J. Microsc. Ultrastruct. 2 (4) (2014) 236, https://doi.org/10.1016/j.jmau.2014.07.001.

[44] W. Tang, Y. Wang, Fractal characterization of impact fracture surface of steel, Appl. Surf. Sci. 258 (10) (2012) 4777–4781, https://doi.org/10.1016/j.apsusc.2012.01.091.

[45] B. VENKATESH, D. CHEN, S. BHOLE, Three-dimensional fractal analysis of fracture surfaces in a titanium alloy for biomedical applications, Scr. Mater. 59 (4) (2008) 391–394, https://doi.org/10.1016/j.scriptamat.2008.04.010.

[46] H. Fu, W. Wang, X. Chen, G. Pia, J. Li, Fractal and multifractal analysis of fracture surfaces caused by hydrogen embrittlement in high-Mn twinning/transformation-induced plasticity steels, Appl. Surf. Sci. 470 (2019) 870–881, https://doi.org/10.1016/J.APSUSC.2018.11.179.

[47] A. Akrami, N. Nasiri, V. Kulish, Fractal dimension analysis of Mg2Si particles of Al–15%Mg2Si composite and its relationships to mechanical properties, Results Mater. 7 (2020) 100118, https://doi.org/10.1016/j.rinma.2020.100118.

[48] W. Macek, R. Branco, M. Szala, Z. Marciniak, R. Ulewicz, N. Sczygiol, P. Kardasz, Profile and Areal Surface Parameters for Fatigue Fracture Characterisation, Materials (Basel) 13 (2020) 3691, https://doi.org/10.3390/ma13173691.

[49] H. Achtelik, M. Kurek, A. Kurek, K. Kluger, R. Pawliczek, T. Lagoda, Non-standard fatigue stands for material testing under bending and torsion loadings, AIP Conf. Proc. (2018), https://doi.org/10.1063/1.5066463.

[50] Z. MARCINIAK, D. ROZUMEK, E. MACHA, Fatigue lives of 18G2A and 10HNAP steels under variable amplitude and random non-proportional bending with torsion loading, Int. J. Fatigue 30 (5) (2008) 800–813, https://doi.org/10.1016/j.ijfatigue.2007.07.001.

[51] K. Slámečka, P. Ponížil, J. Pokluda, Quantitative fractography in bending-torsion fatigue, Mater. Sci. Eng. A 462 (1-2) (2007) 359–362, https://doi.org/10.1016/j.msea.2006.03.153.

[52] H. Achtelik, C.T. Lachowicz, T. “Lagoda, E. Macha, Fatigue characteristics of the notched specimens of 10HNAP steel under cyclic and random synchronous bending with torsion, Proc. 2nd Annu. Fatigue Meet. Copernicus Contract CIPA CT940194, Metz-France, 30-31.08.1996. (1997) 176–191.

[53] D. Rozumek, S. Faszynka, Surface cracks growth in aluminum alloy AW-2017A-T4 under combined loadings, Eng. Fract. Mech. 226 (2020) 106896, https://doi.org/10.1016/j.engfracmech.2020.106896.

[54] Ş. Ţălu, R.S. Matos, E.P. Pinto, S. Rezaee, M. Mardani, Stereometric and fractal analysis of sputtered Ag-Cu thin films, Surf. & Interfaces 21 (2020) 100650, https://doi.org/10.1016/j.surfin.2020.100650.
[55] M. Tanaka, R. Kato, T. Fujita, A. Carpinteri, Y.u. Shouwen, T. Kishi, Review of fractal analysis of fracture surfaces in various materials using three-dimensional images reconstructed by stereo matching method, Strength, Fract. Complex. 12 (2-4) (2020) 143–162, https://doi.org/10.3233/SFC-190244.
[56] A. CARPINTERI, A. SPAGNOLI, S. VANTADORI, An approach to size effect in fatigue of metals using fractal theories, Fatigue Fract. Eng. Mater. Struct. 25 (7) (2002) 619–627, https://doi.org/10.1046/j.1460-2695.2002.00506.x.
[57] W. Macek, T. Łagoda, N. Mucha, Energy-based fatigue failure characteristics of materials under random bending loading in elastic-plastic range, Fatigue Fract. Eng. Mater. Struct. 41 (2) (2018) 249–259, https://doi.org/10.1111/ffe.12677.